

ON THE USE OF X-RAY COMPUTED TOMOGRAPHY FOR MONITORING THE FAILURE OF AN INCONEL 718 TWO-BAR SPECIMEN MANUFACTURED BY LASER POWDER BED FUSION

C. J. Hyde, Z. Xu, A. Thompson, R. K. Leach, I. Maskery, C. J. Tuck & A. T. Clare

Advanced Manufacturing Technology Research Group, University of Nottingham, University
Park, NG7 2RD, United Kingdom

Abstract

Additive manufacturing technologies are highly versatile, capable of producing components with previously impossible complex geometries. However, when additive manufacturing is used to produce parts for critical applications, such as in the aerospace sector, the parts are sometimes limited by poor mechanical properties; largely as a result of porosity and lower material homogeneity than found in, for example, a wrought equivalent. Presented here is a method for identifying material defects, such as porosity, and for monitoring the progress of these defects towards failure during a mechanical test. An Inconel 718 two-bar specimen, produced by laser powder bed fusion, has been applied to a “staged” mechanical test, and X-ray computed tomography used to measure the sample at the end of each “stage”. The X-ray computed tomography data has then been used to provide a history of failure sites prior to failure.

Keywords: Creep, Two-Bar Specimen, X-ray Computed Tomography, Laser Powder Bed Fusion, Inconel 718

Introduction

Laser powder bed fusion (LPBF) is a selective melting additive manufacturing (AM) technology. It is a near-net-shape technique providing a high degree of flexibility in producing potentially complex geometries. Such complex geometries could be, for example, turbine blades. However, the mechanical properties of components manufactured by this technique are yet to be proven satisfactory for some critical applications. Literature shows such efforts to be limited to relatively simple tests, e.g. hardness and tensile testing. Amato et al. [1] studied the effects of the build orientation and post-treatments on the hardness and tensile properties of Inconel 718 samples built in two different atmospheres and confirmed that variations in the mechanical properties were mainly caused by the γ'' precipitates. Jia et al. [2] investigated the effects of changing LPBF build parameters on Inconel 718 samples with an examination of densification, hardness and wear performance. An optimum energy density which resulted in improved mechanical properties was determined. One study, by Rickenbacher et al. [3] showed, for LPBF fabricated IN738LC, that the creep performance of that material was inferior compared to conventionally manufactured samples. However, Pröbstle et al. [4] found Inconel 718 LPBF samples to possess improved creep strength over cast and wrought samples, and that post-process heat treatment further improved the creep performance, although fracture results were not included.

Creep strength/resistance is a key mechanical property for components deployed in high-temperature applications [5], and the use of AM parts here has so far been limited by poor creep performance. Analysis of the response of AM components to creep is, therefore, of critical importance, particularly the response of common defects produced during the AM processes. Conventional creep testing methods do not provide detailed local information on the test specimen but rather bulk behaviour of the material. In this paper, a method for studying defect evolution during a test is presented. Through the use of X-ray computed tomography (XCT) [6], defects can be (non-destructively) detected. In a previously reported study [7], XCT measurement was applied to detect defects in a sample before and after fatigue fracture. Babout et al. [8] used XCT measurements to study the damage mechanisms of room temperature tensile testing of powder metallurgy fabricated samples.

XCT has so far been used for non-destructive testing to measure the spatial distribution of pores in LPBF structures, and a review of such studies is presented by Thompson et al. [9]. Specifically, Maskery et al. [10] successfully quantified and characterized the porosity in LPBF built structures and demonstrated the feasibility of using XCT to give a sufficient description of part porosity, pore size and pore shape. In another study [11], XCT was applied to locate and measure the defects in samples built by selective electron beam melting (SEBM). The novel approach presented in this work combines staged creep testing with XCT and provides new information regarding the creep behaviour of an LPBF built Inconel 718 sample.

Experimental Methodology

An Inconel 718 two-bar small specimen (TBS) was subject to creep testing in this study. The sample was in the as-built condition, with no performance enhancing treatments (e.g. heat treatment, hot iso-static pressing) applied to it. It should be noted that the mechanical performance of the material is not the focus of the presented work and that hot isostatic pressed (HIP) samples are to be tested in subsequent work in order to address this. A TBS (as shown in Fig. 1(b)) is a specimen designed to obtain material creep information from relatively small volumes of material [12]. A raw TBS block (as shown in Fig. 1(a), in which the arrow indicates the LPBF building direction) was built in a Renishaw AM250 LPBF system. The raw block was post-processed using a computer numerical controlled (CNC) milling machine to the specified dimensions (as shown in Fig. 2), as defined by Hyde et al. [12]. Subsequently, creep testing was carried out under stress of 747.45 MPa at a temperature of 650 °C via loading pins on the internal radii of the samples. These parameters were chosen to allow a direct comparison with a study by Sugahara et al. [13] on standard wrought Inconel 718.

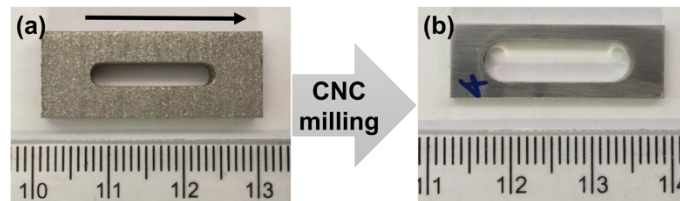


Figure 1: (a) Raw TBS block (arrow indicates the LPBF building direction); (b) CNC machined as-built TBS (dimensions in mm).

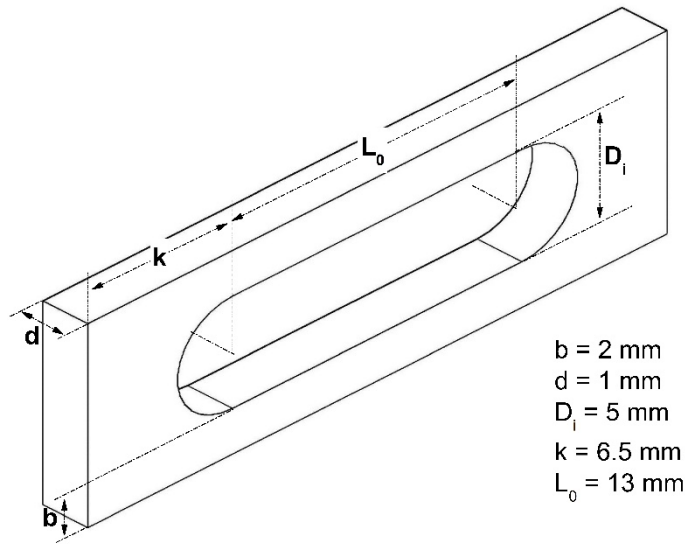


Figure 2: Dimensions of the TBS used in this study [12].

A strategy for staged testing was devised, as shown in Fig. 3. Testing was interrupted when the creep strain reached each pre-set extension. XCT measurements were then performed at these intervals, as well as prior to testing and after failure, yielding four XCT datasets in total.

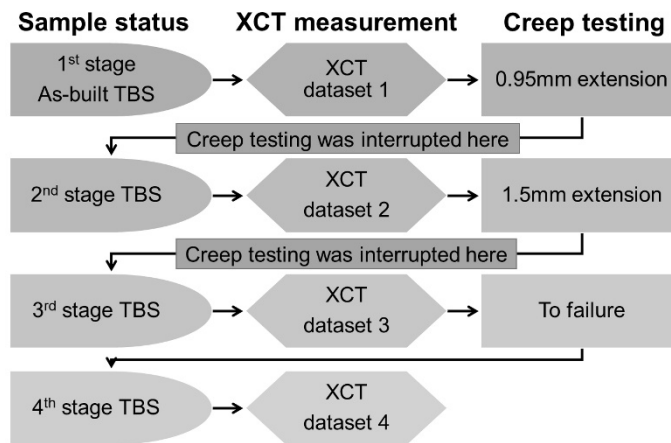


Figure 3: Testing strategy for staged creep testing

A Nikon MCT 225 was used to perform the XCT measurements. Scan parameters were kept constant between measurements, using the following setup: source voltage 225 kV, source current 44 μA , exposure 2000 ms and geometric magnification 20 \times ; yielding a reconstructed voxel size of $10 \mu\text{m} \pm 0.2 \mu\text{m}$ (uncertainty taken from positional variability along the magnification axis between scans). The reconstructed voxel size limits the minimum detectable pore size, as it is generally accepted that the minimum detectable pore size is approximately that of a few voxels. X-ray projections were formed from an average of two frames per projection. A warm up scan of over one hour was performed prior to each scan to minimize the effects of X-ray source fluctuation

as the source temperature stabilized, and a 1.75 mm copper X-ray pre-filter was used. X-ray imaging and volumetric reconstruction were performed using Nikon software (Inspect-X and CT-Pro, respectively), using a filtered back projection reconstruction algorithm with a third order beam hardening correction and a ramp noise filter [14].

Analysis of XCT data was performed on TIFF images outputted in the arrangement shown in Fig. 4, considering only the parallel sections of the sample. The centre of the uniaxial section is set as the zero point; the positive and negative directions are marked in Fig. 4. All descriptions in the following are based on this convention. Image stack analysis was performed using a combination of MATLAB [15] and ImageJ [16]. The ISO 50 surface determination method [17] was initially applied to threshold image stacks. However, in this case, the threshold ISO 50 grey value provided clearly spurious thresholding results. The thresholding value was manually adjusted to ISO 78.6 to provide a clear representation of pores in a number of example images while minimizing noise in the binarized images. The ISO 78.6 threshold was then applied to all images individually using MATLAB. The binary images produced by MATLAB were then analysed using ImageJ to calculate porosity, pore size and standard distribution metrics. In order to filter any remaining noise and focus only on the largest pores, areas larger than 20 pixels (which is five times larger than that used in previous work [8]) in the binarized images were treated as pores. This area is five times larger than that used in previous work [10], but was chosen in order to ensure complete noise filtration for comparison between test stages. This filtration is necessary as determining between the smallest pores and noise is highly complex, and can reduce the robustness of calculated porosities, which is essential for comparison purposes.

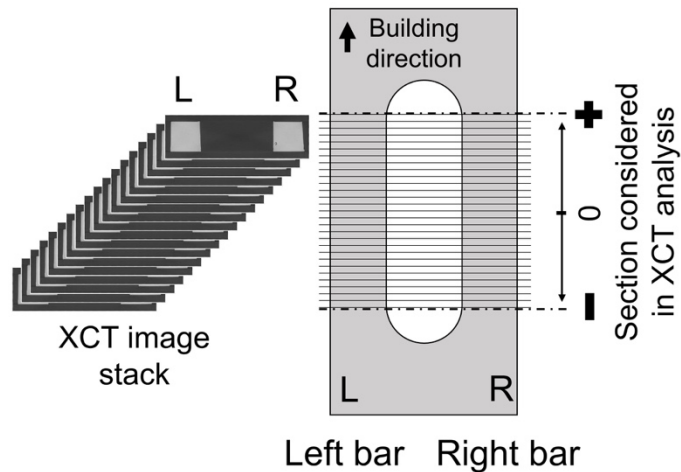


Figure 4: XCT image stacking and the convention for referencing scanned position

Results

Staged creep testing results

Table 1 shows the results of the staged test. The 2nd and 3rd stages have short experimental times and were effectively high-temperature tensile testing/initial straining.

Table 1: Results of all three stages of the staged creep testing

	Pre-set extension /mm	Real extension /mm	Experimental time /s
2nd stage TBS	0.950	0.430	23.19
3rd stage TBS	1.500	0.400	39.7
4th stage TBS	To failure	0.714	41400
<i>Total</i>	<i>To failure</i>	<i>1.544</i>	<i>41462.89</i>

XCT measurements

The cross-sectional area of the TBS specimen was calculated from each image in the image stack during the first three XCT measurement stages (i.e. the 1st stage, 2nd stage and 3rd stage, shown in Fig. 5). The cross-sectional area along the TBS parallel regions decreased notably during creep testing. Also, ‘valleys’ present at both ends of the gauge section during the 2nd and 3rd stages indicated likely fracture position/s in the sample.

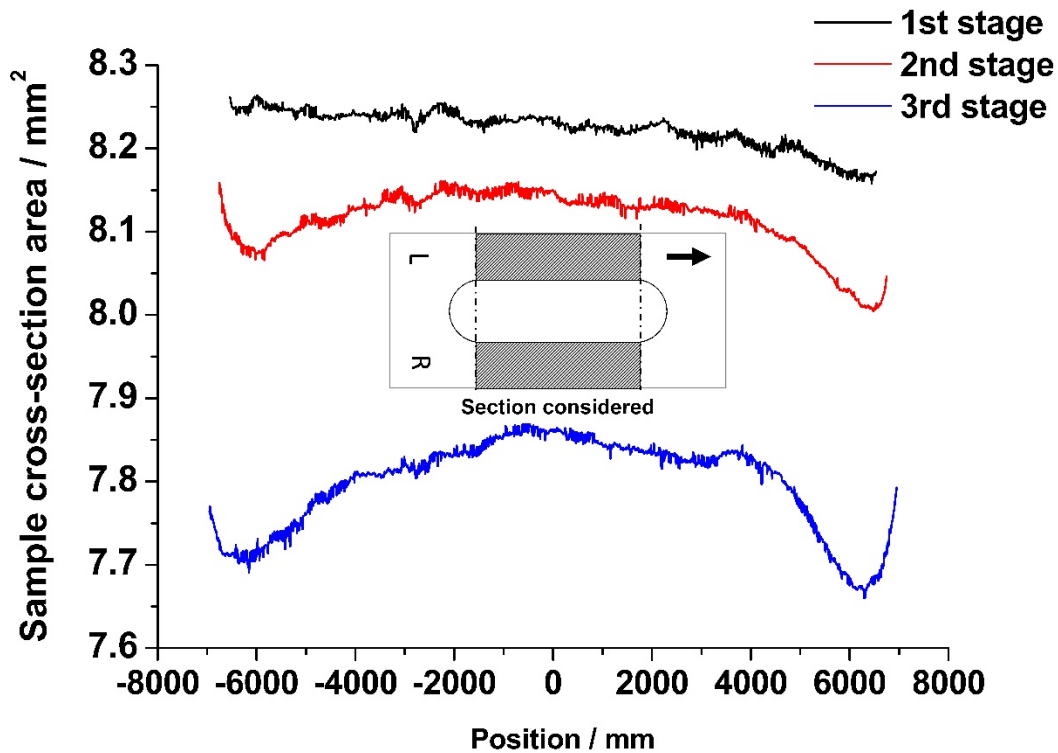


Figure 5: Using XCT, the cross-sectional area as a function of position along the TBS can be computed.

Porosity distributions in the three XCT stages along the uniaxial section are shown in Fig. 6, where increasing porosity across the three stages, most dramatically in the 3rd stage, can be observed.

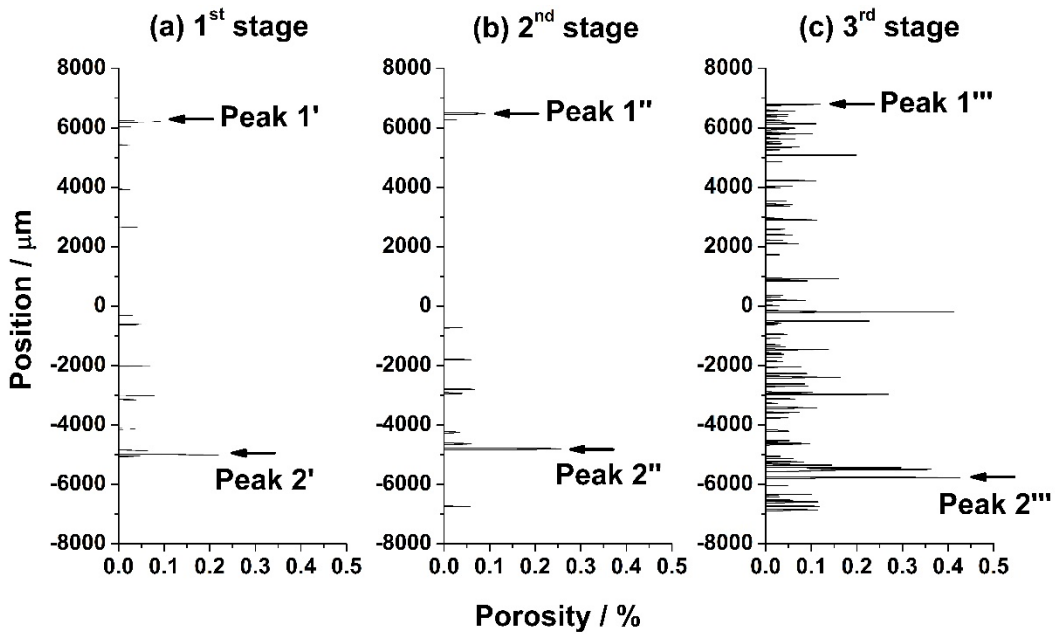


Figure 6: Porosity variation along the building direction including both bars of the TBS (a) 1st stage; (b) 2nd stage; (c) 3rd stage.

As shown in Fig. 7, the porosity distribution in the left and right bars of the TBS differs noticeably, likely as a result of the random distribution of the defects appearing during the LPBF process.

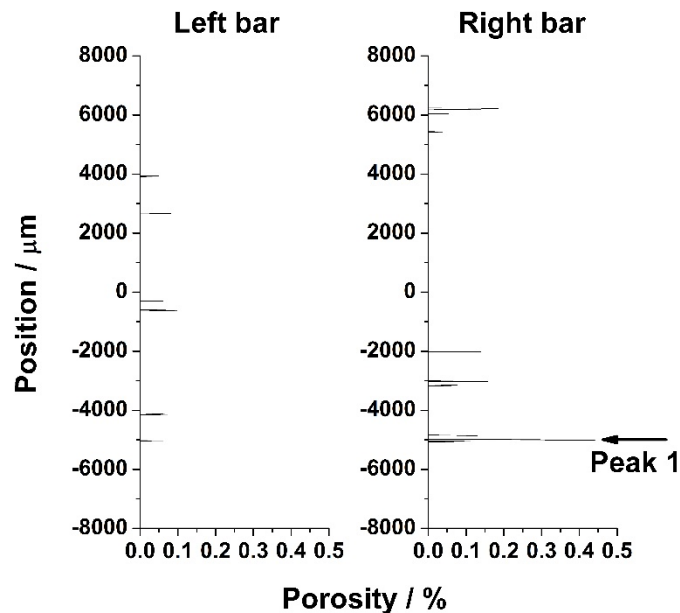


Figure 7: Comparison of the porosity variation along the build direction between the left and right bars of the TBS before creep testing.

Comparing the porosity distribution in the two bars, it is possible to predict that the failure will most likely be observed in the bottom section (marked by Peak 1 in Fig. 7) of the right bar.

Fracture analysis

The sample was also examined following fracture. The fracture section itself was ignored when calculating the porosity distribution since it is difficult to distinguish the pore from the background.

By comparing the porosity distribution in all four stages, it is clear that the largest peak present in the first three stages represents the ultimate position of failure of the sample. This peak was no longer observable in the 4th stage, as shown in Fig. 8(d), as this is the position of the fracture surface. When examining the XCT data, it is possible to pinpoint the specific pores from which the eventual failure originated. 3D models of the pores in question (shown parts (a), (b) and (c) of Fig. 9) were obtained by assembling XCT orthoslices to provide additional understanding of how the defects in the eventual fracture section evolved during the creep test. Fig. 9(d) shows the SEM image of the interior of the pores which were pinpointed in the 3rd stage, as shown in Fig. 9(c).

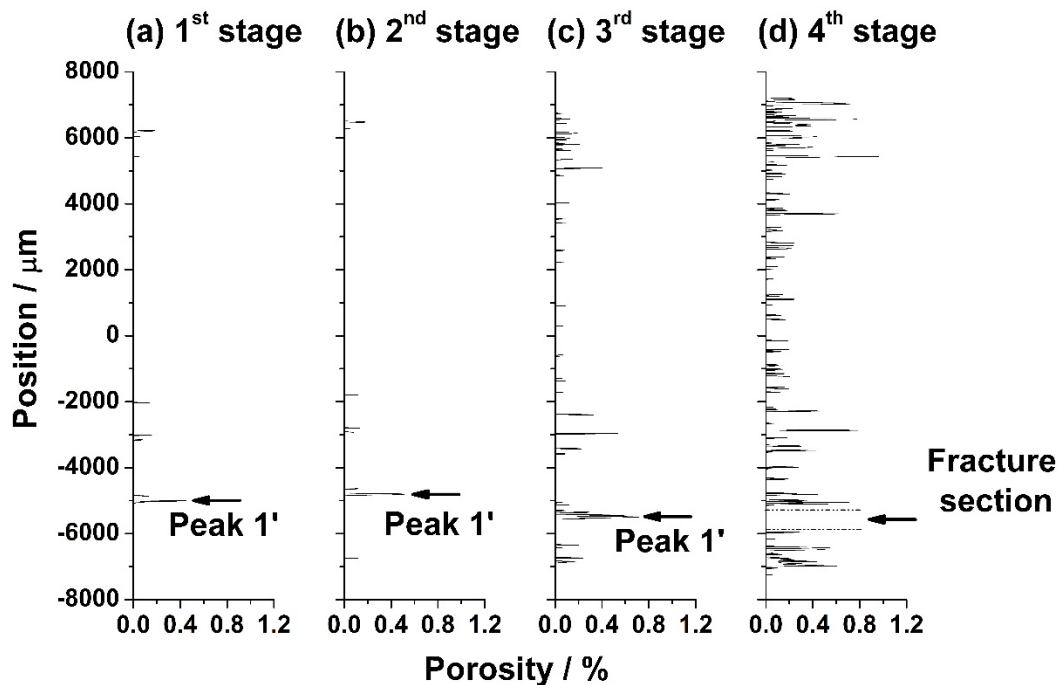


Figure 8: Porosity variation along the building direction in the right bar: (a) 1st stage; (b) 2nd stage; (c) 3rd stage; (d) 4th stage

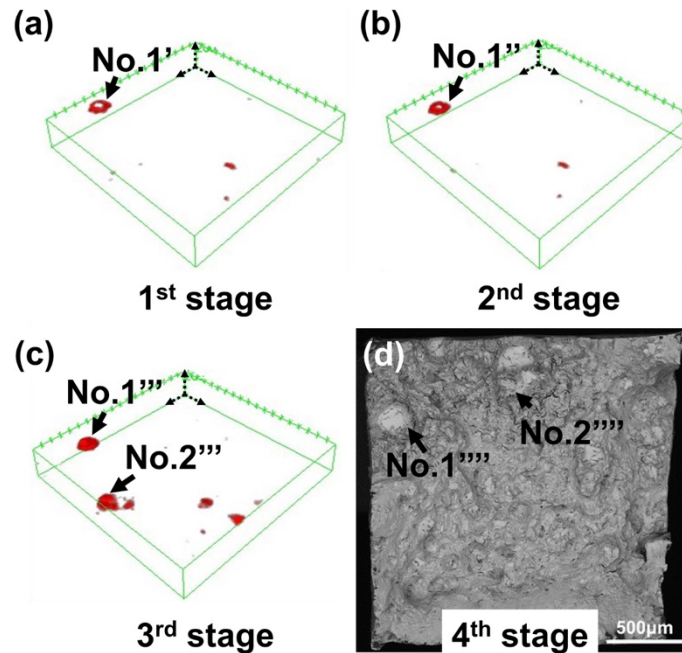


Figure 9: Visualizations of the evolution of defects in the fracture section in all four stages of the creep test: (a) 1st stage (XCT model); (b) 2nd stage (XCT model); (c) 3rd stage (XCT model); (d) 4th stage (SEM image).

Discussion and Conclusions

Staged creep testing

The short experimental times involved in the presented test indicate that a large proportion of the extension observed is initial straining and may still be in the elastic regime. Thus, extensions were smaller than expected. The fracture surface of the staged tested sample shows a creep dominated failure mechanism. Should the testing be repeated, it may be reasonable to separate the stages by time, rather than extension, in order to allow the creep mechanism to be fully developed before the first stage interruption of the test.

XCT measurements have resulted in direct evidence of randomly distributed defects generated during the LPBF process, with higher porosity than some other conventional (e.g. wrought) methods. These inbuilt defects are the result of a combination of the scanning strategy, the part geometry and the powder quality. The larger pores cause a weakness of the sample and may act as fracture initiation points in the subsequent testing.

With regard to the entire uniaxial section, an obvious decrease in the cross-sectional area was observed during the test, with the two ends of the gauge section being found to have a higher area reduction compared to the mid-section, indicating that these two positions are the most porous sections in the tested samples. Therefore, fracture is most likely to occur at these positions. As can be seen in Fig. 5, the two ends have 30% more area reduction compared with the midpoint in the 3rd stage when taking the non-crept sample as a benchmark.

Apart from the changes in the cross-sectional area, the porosity distributions also show the increase of the defects in the sample.

The 3rd stage XCT analysis showed the highest porosity and indicates that the sample is much closer to failure at this stage than in the first two stages. Also, the growth of the number of pores seems to play a more important role than the growth of the pore size in the later stage.

By analyzing the porosity distribution of the fractured sample, the origin of the first fracture can be pinpointed. Since it is not possible to calculate the porosity in the fracture section immediately before failure, its porosity distribution is not shown. It is also noted that the highest peak in porosity observed in the first three XCT stages cannot be observed in the 4th stage due to fracture occurring in this position. 3D models are shown and clearly illustrate the evolution of the defects in the fracture section. Pore No.1 is observed to grow during the creep testing and a group of new pores generated in the 3rd stage are shown.

Acknowledgements

The authors would like to acknowledge the support from Engineering and Physical Sciences Research Council (EPSRC Grants EP/L017121/1). Thanks are also given to Renishaw for the contribution of test samples. In addition, the authors would like to thank Alexander Jackson-Crisp for his invaluable technical contributions in machining specimens, Shane Maskill for facilitating the creep testing and to Renishaw Plc, process engineering team for providing Inconel 718 samples. AT and RKL would like to thank EPSRC (Grants EP/M008983/1 and EP/L01534X/1) and 3TRPD Ltd. for funding this work.

References

- [1] K. N. Amato, S. M. Gaytan, L. E. Murr, E. Martinez, P. W. Shindo, J. Hernandez, S. Collins & F. Medina, “Microstructures and mechanical behavior of Inconel 718 fabricated by LPBF”, *Acta Materialia* **60**(5), 2012, pp 2229-2239.
- [2] Q. Jia & D. Gu, “LPBF additive manufacturing of Inconel 718 superalloy parts: Densification, microstructure and properties”, *Journal of Alloys and Compounds* **585**, 2014, pp 713-721.
- [3] L. Rickenbacher, T. Etter, S. Hövel & K. Wegener, “High temperature material properties of IN738LC processed by LPBF (LPBF) technology”, *Rapid Prototyping Journal* **19**(4), 2013, pp 282-290.
- [4] M. Pröbstle, S. Neumeier, J. Hopfenmüller, L. P. Freund, T. Niendorf, D. Schwarze & M. Göken, “Superior creep strength of a nickel-based superalloy produced by LPBF”, *Materials Science and Engineering: A* **674**, 2016, pp 299-307.

- [5] S. F. Diltemiz & S. Zhang, “Superalloys for super jobs”, in: S. Zhang & D. Zhao (Eds.), *Aerospace Material Handbook*, CRC Press, London, 2013, pp 1-76.
- [6] J. Hsieh, “Computed tomography: principles, design, artifacts, and recent advances”, Bellingham, WA, USA: SPIE Press, 2009.
- [7] Y. Hangai, O. Kuwazuru, T. Yano, T. Utsunomiya, Y. Murata, S. Kitahara, S. Bidhar & N. Yoshikawa, “Clustered shrinkage pores in Ill-conditioned aluminum alloy die castings”, *Materials Transactions* **51**(9), 2010, pp 1574-1580.
- [8] L. Babout, E. Maire, J. Y. Buffière & R. Fougères, “Characterization by X-ray computed tomography of decohesion, porosity growth and coalescence in model metal matrix composites”, *Acta Materialia* **49**(11), 2001, pp 2055-2063.
- [9] A. Thompson, I. Maskery & R. K. Leach, “X-ray computed tomography for additive manufacturing: a review”, *Measurement Science and Technology* **27**(7), 2016, pp 1-17.
- [10] I. Maskery, N. T. Aboulkhair, M. R. Corfield, C. Tuck, A. T. Clare, R. K. Leach, R. D. Wildman, I. A. Ashcroft & R. J. M. Hague, “Quantification and characterisation of porosity in selectively laser melted Al–Si10–Mg using X-ray computed tomography”, *Materials Characterization* **111**, 2016, pp 193-204.
- [11] S. Tammas-Williams, H. Zhao, F. Léonard, F. Derguti, I. Todd & P. B. Prangnell, “XCT analysis of the influence of melt strategies on defect population in Ti–6Al–4V components manufactured by Selective Electron Beam Melting”, *Materials Characterization* **102**, 2015, pp 47-61.
- [12] T. H. Hyde, B. S. M. Ali & W. Sun, “Analysis and design of a small, two-bar creep test specimen”, *Journal of Engineering Materials and Technology* **135**(4), 2013.
- [13] T. Sugahara, K. Martinolli, D. A. P. Reis, C. de Moura Neto, A. A. Couto, F. P. Neto & M. J. R. Barboza, “Creep behavior of the Inconel 718 superalloy”, *Defect and Diffusion Forum* **326-328**, 2012, pp 509-514.
- [14] H. Jiang, “Image reconstruction, computed tomography principles, design, artifacts, and recent advances”, SPIE Press, Bellingham, USA, 2009.
- [15] O. Marques, “Image segmentation, practical image and video processing using MATLAB”, Wiley, Hoboken, New Jersey, 2011, pp 368-370.
- [16] C. A. Schneider, W.S. Rasband & K.W. Eliceiri, “NIH Image to ImageJ: 25 years of image analysis”, *Nature Methods* **9**(7), 2012, pp 671-675.
- [17] J. P. Kruth, M. Bartscher, S. Carmignato, R. Schmitt, L. De Chiffre, A. Weckenmann, “Computed tomography for dimensional metrology”, *CIRP Annals - Manufacturing Technology* **60**(2), 2011, pp 821-842.